PNAS RESEARCH ARTICLE | PHYSICS

Sensing ultrashort electronic coherent beating at conical intersections by single-electron pulses

Shahaf Asban[a,b,1], Daniel Keefer[a,b], Vladimir Y. Chernyak[c,d,1], and Shaul Mukamel[a,b,1]

Contributed by Shaul Mukamel; received March 29, 2022; accepted April 19, 2022; reviewed by Marcos Dantus and Thomas Elsaesser

Consolidation of ultrafast optics in electron spectroscopies based on free electron energy exchange with matter has matured significantly over the past two decades, offering an attractive toolbox for the exploration of elementary events with unprecedented spatial and temporal resolution. Here, we propose a technique for monitoring electronic and nuclear molecular dynamics that is based on self-heterodyne coherent beating of a broadband pulse rather than incoherent population transport by a narrowband pulse. This exploits the strong exchange of coherence between the free electron and the sample. An optical pulse initiates matter dynamics, which is followed by inelastic scattering of a delayed high-energy broadband single-electron beam. The interacting and noninteracting beams then interfere to produce a heterodyne-detected signal, which reveals snapshots of the sample charge density by scanning a variable delay T. The spectral interference of the electron probe introduces high-contrast phase information, which makes it possible to record the electronic coherence in the sample. Quantum dynamical simulations of the ultrafast nonradiative conical intersection passage in uracil reveal a strong electronic beating signal imprinted onto the zero-loss peak of the electronic probe in a background-free manner.

conical intersections | single-electron spectroscopy | ultrafast dynamics

Significance

In a theoretical study, we present an ultrafast technique for probing time-dependent molecular charge densities. An ultrafast optical pump first brings the molecule into an electronic nonstationary state. This is followed by coherent inelastic scattering of a broadband single-electron probe pulse with a variable delay T, which is detected spectrally. The technique is applied to reveal phase-sensitive background-free coherent electron beating in the conical intersection passage in uracil and reveals the otherwise elusive coherent beating of strongly coupled electrons and nuclei.

Strongly coupled electronic and nuclear motions in molecules give rise to ultrafast relaxation pathways, some of which are optically dark. State-of-the-art single-electron microscopes equipped with ultrafast optical elements introduce hybrid probes involving both electrons and photons. In this theoretical study, we show that when a broadband fast electron (~ 0.3MeV) passes near an optically pumped molecule, an interference between the interacting and noninteracting free electron trajectories stores information regarding inelastic scattering in the transmitted electron spectrum. This single-pulse inelastic coherent electron scattering (SPICES) technique is demonstrated for the conical intersection (CoIn) passage with joint nuclear–electronic contributions in the RNA base uracil.

Several experimental techniques (1–5) have been proposed for monitoring ultrafast charge-density dynamics by combining electron microscopy with advanced ultrafast optics, pioneered by Zewail and coworkers (1, 3, 4). Photon-induced near-field electron microscopy (1, 3–5) acquires temporal resolution via the embedded ultrafast optics in electron microscopes. The temporal resolution is achieved by scanning the controlled delay time between the optical pump and the interaction with a passing electron. Another electron spectroscopy technique is electron energy loss spectroscopy (EELS)/electron energy gain spectroscopy, which is usually formulated for macroscopic samples (2, 5). Both techniques derive their spectral resolution from the narrow energy distribution of the electron beam. The electron probe undergoes inelastic scattering and may lose or gain energy when coupled to the optically pumped macroscopic sample. These inelastic processes can be observed by spectrally dispersing the probe. In the macroscopic description, both methods are sensitive to sample geometry and the populated plasmonic modes. Matter spectroscopic information is imprinted into plasmon populations using the imaginary part of the response to the applied electromagnetic field. The latter is used as a source to which the linear response typically applies (6–8).

In this paper, we introduce the SPICES signal and show that when the sample is prepared by a resonant pump, a single interaction with the electronic probe generates a coherent signal. The interference induced in the incoming beam is analogous to heterodyne detection of photons for comparison. Conventional EELS requires at least two interactions to populate new energy states of the probe. The SPICES setup is composed of the inelastic electron scattering process depicted in Fig. 1. At $t = 0$, the sample is optically excited by a short optical pulse, launching electronic and nuclear dynamics. A high-energy electron beam (a few hundred kiloelectron volts) with a typical full-width at half-maximum (FWHM) $\propto 300$ fs and mean velocity v then recoils along the longitudinal (z)

Author affiliations: [a]Department of Chemistry, University of California, Irvine, CA 92697-2025; [b]Department of Physics & Astronomy, University of California, Irvine, CA 92697-2025; [c]Department of Chemistry, Wayne State University, Detroit, MI 48202; and [d]Department of Mathematics, Wayne State University, Detroit, MI 48202

Author contributions: S.A. and D.K. designed research; S.A. and D.K. performed research; V.Y.C. contributed new reagents/analytic tools; S.A. and D.K. analyzed data; and S.A., D.K., and S.M. wrote the paper.

Reviewers: M.D., Michigan State University; and T.E., Max Born Institut fur Nichtlineare Optik und Kurzzeitspektroskopie im Forschungsverbund Berlin eV.

The authors declare no competing interest.

[1]To whom correspondence may be addressed. Email: sasban@uci.edu, chernyak@chem.wayne.edu, or smukamel@uci.edu.

This article contains supporting information online at https://www.pnas.org/lookup/suppl/doi:10.1073/pnas.2205510119/-/DCSupplemental.

Published May 24, 2022.

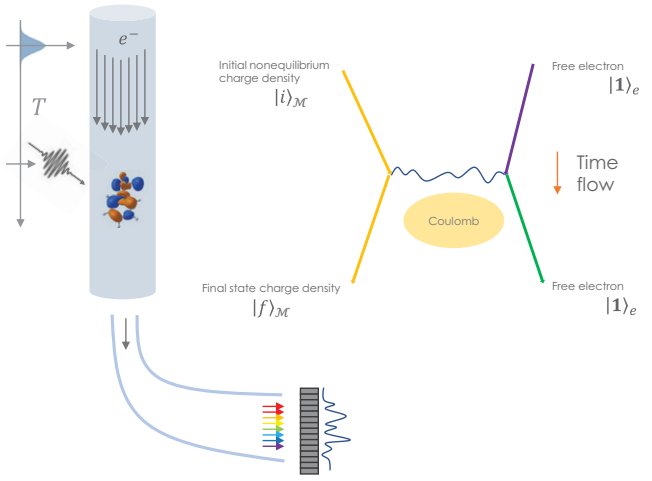

Fig. 1. The setup. (*Left*) A sample is optically pumped at $t = 0$ into a transient state. A broadband single-electron pulse temporally centered at $t = T$ is then coupled to the sample, exchanging momentum with the sample. The spectral profile of the electron is detected. (*Right*) Diagrammatic representation of the electron coupling.

direction by the long-range Coulomb interaction with the sample. The scattered electron pulse initially centered at a variable delay $t = T$ is energy dispersed. The process is described by the loop diagram in Fig. 2. The spectrally resolved electron is derived in *SI Appendix*, section I, which yields the SPICES signal

$$\mathcal{S}_{\boldsymbol{k}}(T) = \frac{2e}{\hbar\gamma}\mathrm{Re}\int_{-\infty}^{\infty}\frac{d\omega}{2\pi}e^{-i\omega T} \times\int_{\mathbb{R}^3}\frac{d\boldsymbol{q}}{(2\pi)^3}\frac{\sigma_\mu(\boldsymbol{q},\omega)}{\boldsymbol{q}^2}\frac{1}{\boldsymbol{v}_{\boldsymbol{k}}\cdot\boldsymbol{q}-\omega+i\gamma}\phi_{\boldsymbol{k}-\boldsymbol{q}}\phi^*_{\boldsymbol{k}}, \quad [1]$$

where σ_μ is the total molecular charge density, $\phi_{\boldsymbol{k}}$ is the free electron amplitude, $\boldsymbol{k}$ is the detected electron momentum related to the energy–momentum exchange via $\omega = \boldsymbol{q}\cdot\boldsymbol{v}_{\boldsymbol{k}} = \frac{\hbar}{m}\boldsymbol{k}\cdot\boldsymbol{q}$, and $\boldsymbol{v}_{\boldsymbol{k}}$ is the corresponding free electron velocity. The SPICES signal scales $\propto q^{-2}$ rather than the q^{-4} for conventional incoherent (narrowband) EELS (9).

Here, our primary goal is spectroscopy rather than microscopy. To that end, we utilize a collimated, unfocused electron rather than a tightly focused beam as used when spatial information is desired. This offers insights into the molecular dynamics thanks to the high-contrast information delivered by the hybrid probe regarding the strong nuclei–electron coupling.

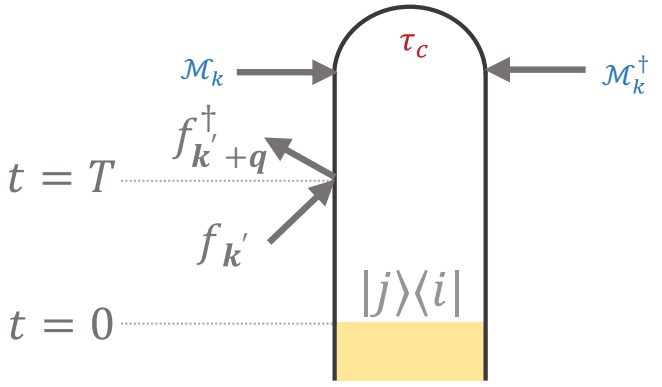

Fig. 2. Loop diagram representation of SPICES. The time flows in a loop from $-\infty$ (on the lower left) to t at the top of the loop and then, backward to $-\infty$ (on the lower right). The sample is initially prepared in a transient state during $t \in (-\infty, 0)$ represented by the yellow box (on the bottom). An electron beam centered at $t = T$ scatters from momentum state $\mathbf{k} \to \mathbf{k} + \mathbf{q}$. Finally, an electron is detected, represented by the two inward arrows at the top of the loop diagram and the corresponding measurement operators $\mathcal{M}_k\left(\mathcal{M}_k^\dagger\right)$.

Results and Discussion

The Setup. The system is described by the Hamiltonian $\mathcal{H} = H_\varphi + H_f + H_\mu + H_I$, composed of the electromagnetic field (φ), free electron (f), matter (μ), and interaction (I) contributions. The free electron's Hilbert space is assumed to be separable from the matter, excluding exchange pathways from the physical discussion. The interaction Hamiltonian of the sample with the electron field is given by

$$H_I = -\frac{e\hbar}{mc}\int d^3r\boldsymbol{j}(\boldsymbol{r})\cdot\boldsymbol{A}(\boldsymbol{r}) - \frac{e^2}{2}\int d^3r d^3R\frac{\sigma_f(\boldsymbol{r}+\boldsymbol{R})\sigma_\mu(\boldsymbol{r})}{|\boldsymbol{R}|}, \quad [2]$$

where we have used the Coulomb gauge for the electromagnetic vector potential $\mathbf{A}(\mathbf{r})$. σ_f and σ_μ represent the free electron and sample charge-density operators, respectively. The single free electron is described by the wave packet $|\mathbf{1}_e\rangle = \sum_{\boldsymbol{p}}\phi_{\boldsymbol{p}}f^\dagger_{\boldsymbol{p}}|\emptyset\rangle$, where $\phi_{\boldsymbol{p}}$ is the single-electron amplitude, $|\emptyset\rangle$ is the free electron vacuum, and $f^\dagger_{\boldsymbol{p}}$ $(f_{\boldsymbol{p}})$ is a free (spinless) electron creation (annihilation) operator obeying Fermion anticommutators $\left\{f_{\boldsymbol{p}}, f^\dagger_{\boldsymbol{p}'}\right\} = \delta_{\boldsymbol{p}\boldsymbol{p}'}$. Gauge fixing is crucially important for the physical interpretation of the detected quantities. Note that the interactions of the bound electrons and nuclei are included in H_μ. The free electron and matter are initially uncorrelated, and their wave functions are thus factorized.

The free electron measurement is represented by instantaneous annihilation of a momentum state using the electron operator $f_{\mathbf{k}}$ within an energy window $m_{\mathbf{k},\mathbf{k}'}$, given by $\mathcal{M}_{\mathbf{k}}(t) = \int d\boldsymbol{k}' m_{\mathbf{k},\mathbf{k}'}f_{\mathbf{k}'}(t)$. These operators are defined by the measurement setup and the detector properties. The signal is given by the integrated current with momentum $\mathbf{k}$:

$$\mathcal{S}_{\mathbf{k}}(T) = \int dt\,\delta\mathcal{I}_{\mathbf{k}}(t), \quad [3]$$

where $\delta\mathcal{I}_k = \left\langle\Phi(t)\left|\mathcal{I}^{(\mathrm{int})}_{\mathbf{k}} - \mathcal{I}_0\right|\Phi(t)\right\rangle$ is the change in the free electron spectral density due to the interference of the interacting and noninteracting contributions. $\mathcal{I}_0$ is the initial spectral density of the probe, $\mathcal{I}^{(\mathrm{int})}_{\mathbf{k}}$ represents the interaction with the sample, and $|\Phi(t)\rangle$ is the joint electron plus sample wave function. We expand the joint electron–sample wave function in powers of the interaction Hamiltonian (2). In the Coulomb gauge, the vector field $\boldsymbol{A}(\boldsymbol{r})$ does not contribute to first order since the electromagnetic field for $T > 0$ is in its vacuum state. The coupling is thus solely given by the Coulomb term $H_I = -\frac{e^2}{2}\int d^3r d^3R\frac{\sigma_f(\boldsymbol{r}+\boldsymbol{R})\sigma_\mu(\boldsymbol{r})}{R}$. Eq. **1** is obtained by using 1) high spectral resolution $m_{k,k'}$ such that $v\Delta k \ll \gamma$ (*SI Appendix*, section I), and 2) the energy exchange between the sample and electron is much smaller than the free electron central momentum $\boldsymbol{k}_i \gg \boldsymbol{q}$ such that $\varepsilon_{\boldsymbol{k}+\boldsymbol{q}} \approx \varepsilon_{\boldsymbol{k}} + \boldsymbol{v}_{\boldsymbol{k}}\cdot\boldsymbol{q}$, where $\boldsymbol{v}_{\boldsymbol{k}} = \frac{\hbar}{m}\boldsymbol{k}$ and $\hat{k} \parallel \hat{z}$.

Eq. **1** includes the free electron amplitude $\phi_{\mathbf{k}}$, reflecting the self-heterodyning interference between noninteracting and interacting electron states. Only transitions within the electron's bandwidth are recorded. In the single-electron regime considered here, the effective electron bandwidth characterized by the FWHM $\Delta\varepsilon$ is determined by several factors. One important factor is the match

between the energy of the ionizing photon $\hbar\omega_p$ and the cathode work function Φ (10). By tuning this parameter $\alpha = \hbar\omega_p - \Phi$, a reduction of the electron energy distribution was reported in both the longitudinal and transverse momentum components (11). Minimal broadening values of $\Delta\varepsilon/\varepsilon \in \{10^{-5}, 10^{-6}\}$ have been realized (including acceleration-induced broadening) in the range of 30 to 300 keV (11). Our proposed measurement benefits from a broad energy spread, for which α can be tuned.

Monitoring the Nonadiabatic Dynamics. The time-dependent wave function of the optically pumped sample can be expanded in a superposition in the adiabatic basis:

$$\Psi(\mathbf{r}, \mathbf{R}, t) = \sum_i c_i(t)\, \varphi_i(\mathbf{r}, \mathbf{R})\, \chi_i(\mathbf{r}, \mathbf{R}). \qquad [4]$$

Here, $\varphi_i(\mathbf{r}, \mathbf{R})$ is the ith electronic state; $\chi_i(\mathbf{r}, \mathbf{R})$ is the corresponding nuclear wave packet; $\mathbf{r}$ and $\mathbf{R}$ are electronic and nuclear positions, respectively; and $c_i(t)$ is its time-dependent amplitude due to the optical pumping. Eq. **1** can be expressed explicitly:

$$\mathcal{S}(\mathbf{k}, T) \propto \Im\mathfrak{m}\left\{ \int dt\, d\mathbf{q} e^{i\frac{\hbar}{m}\mathbf{k}\cdot\mathbf{q}(T-t)} \frac{\phi_{\mathbf{k}-\mathbf{q}}\phi^*_{\mathbf{k}}}{q^2} \right. \qquad [5]$$
$$\left. \times \sum_{ij} \rho^*_{ij}(t) \langle \chi_i(t) | \hat{\sigma}(\mathbf{q}) | \chi_j(t) \rangle \right\},$$

where $\rho_{ij}(t) = c_i(t)\, c^*_j(t)$ is the electronic coherence and $\hat{\sigma}(\mathbf{q})$ is the Fourier transform of the total charge density. The charge-density operator $\sigma = \sigma_e + \sigma_n$ (electron plus nuclei) is assumed to be diagonal in the nuclear space (no coherence), and the momenta $\{\mathbf{k}, \mathbf{q}\}$ are parallel to the electron trajectory (here, the $\hat{z}$ axis by convention).

Application to the CoIn Passage in Uracil.

CoIns. CoIns are degeneracy regions between electronic potential energy surfaces of molecules. Around CoIns, the electronic and nuclear frequencies are comparable and strongly coupled. Thus, they play an essential role in photochemistry, enabling ultrafast nonradiative relaxation pathways (<100 fs). This renders them strong candidates for energy conversion and switching applications that rely on CoIns as their operational principle. Moreover, CoIns offer control knobs over product yields and rates of a large class of photochemical processes (reviewed in ref. 12). Numerous photoinduced reactions enabled by CoIns have been studied, such as cyclohexadiene ring opening (13), photosynthesis of vitamin D (14), retinal photoisomerization in the primary event of vision (15), photodamage of DNA (16), and DNA repair (17). Due to their high quantum yield and ultrafast switching, optical molecular switches that rely on CoIns have been proposed for numerous applications ranging from optical memories to chemical energy storage (18, 19). From the theoretical perspective, CoIns are exceptionally interesting since the electronic and nuclear motions are strongly coupled and thus, inseparable [beyond the Born–Oppenheimer approximation (20)]. Spectroscopically, direct detection of CoIns is a daunting challenge since the associated signatures—based on coherences rather than populations—are intrinsically weak. Here, we show how the direct detection of CoIns is possible by using pulsed electrons.

Application to uracil. Our model is based on ab initio multireference quantum chemical data on the photorelaxation of the RNA nucleobase uracil (21) that is crucially relevant for RNA photostability. An effective Hamiltonian that includes two nuclear degrees of freedom is constructed. The latter captures the relaxation through a CoIn after the optical excitation with kinetic rates that match corresponding experiments (22). Exact nonadiabatic quantum dynamical propagation of the photoexcited wave packet is performed, fully capturing the quantum character of the nuclei and therefore, the CoIn passage. The Hamiltonian, along with analysis of the wave packet motion, has been described in detail elsewhere (21, 23). Briefly, a 20-fs FWHM optical pump pulse, resonantly tuned to the electronic $S_0 \rightarrow S_2$ transition, launches a nuclear wave packet in the S_2 excited state. After a short free evolution period, it reaches the S_2/S_1 CoIn around 100 fs and relaxes to S_1. This generates a vibronic coherence between S_2 and S_1 due to the nonvanishing overlap of the nuclear wave packet in the two states. Small parts of the wave packet continue to reach the CoIn, and it takes several hundred femtoseconds for the relaxation to be completed. The population and coherences dynamics are depicted in Fig. 3 *A–C* and in Fig. 3 *D–F*, respectively.

The average beam momentum (k_0) introduces fast oscillation in Eq. **5**, from which the relevant integration time can be inferred. When the electron's velocity is approximately half the speed of light in vacuum $v_0 \approx 0.5c$, these oscillations determine the temporal resolution $\delta T \equiv t - T$, which depends on the observed momenta exchange with the sample. The longitudinal momenta exchange, parallel to the electron propagation direction $(\mathbf{q} \parallel \mathbf{k})$, determines the significant integration interval—here, collimated and thus, quasione dimensional. For momentum exchange $\mathbf{q}$ in the range of several inverse angstroms $\left(10^{-10}\mathrm{m}\right)$, the effective temporal width of the probe is $\delta T > 10^{-18}$ s. It is, therefore, reasonable to estimate the temporal resolution within the order of 0.1 fs, which is lower than the time step used for the numerical calculations $\Delta t_{\mathrm{sim}} = 0.48$ fs. Assuming that within these time steps, the charge density does not vary significantly, the temporal summation can be replaced by sampling the charge density at $t = T$. This assumption is validated by our numerical calculation of the temporal dynamics. In this parameter regime, the signal is given by

$$\mathcal{S}_{\mathbf{k}}(T) \propto \Im\mathfrak{m}\left\{ \int d\mathbf{q} \frac{\phi_{\mathbf{k}-\mathbf{q}}\phi^*_{\mathbf{k}}}{q^2} \right. \qquad [6]$$
$$\left. \times \sum_{ij} \rho^*_{ij}(T) \langle \chi_i(T) | \hat{\sigma}(\mathbf{q}) | \chi_j(T) \rangle \right\}$$
$$\equiv \sum_{ij} \mathcal{S}_{ij}(\mathbf{k}, T).$$

Eq. **6** is derived from Eq. **1** by performing the Fourier transform of the charge density to time domain and integrating the radial frequency ω for small γ followed by eliminating the fast oscillating contributions with respect to the resolution as discussed above (Eq. **5**).

Fig. 4 depicts the various contributions $\mathcal{S}_{ij}(\mathbf{k}, T)$ defined in Eq. **6**. Fig. 4 *A–C* captures the population dynamics, and the electronic coherences are given in Fig. 4 *D–F*. From Eq. **6**, we can appreciate that low momenta values contribute significantly to the signal due to the $\mathbf{q}^{-2}$ weight. This corresponds to long-wavelength dominance, similar to the general form of transient redistribution of ultrafast electronic coherences in attosecond Raman signals (TRUECARS) introduced in ref. 24. TRUECARS is dominated by the polarizability and generated by the longitudinal component of the off-resonant X-ray scattering that follows optical excitation. Here, the long wavelength of the electronic charge density plays a similar role to the one of the polarizability in the TRUECARS signal. From Fig. 4, it is clear that electronic population contribution to the signal is antisymmetric and vanishes exactly at $k = k_0$, which stems from the fact that this is a

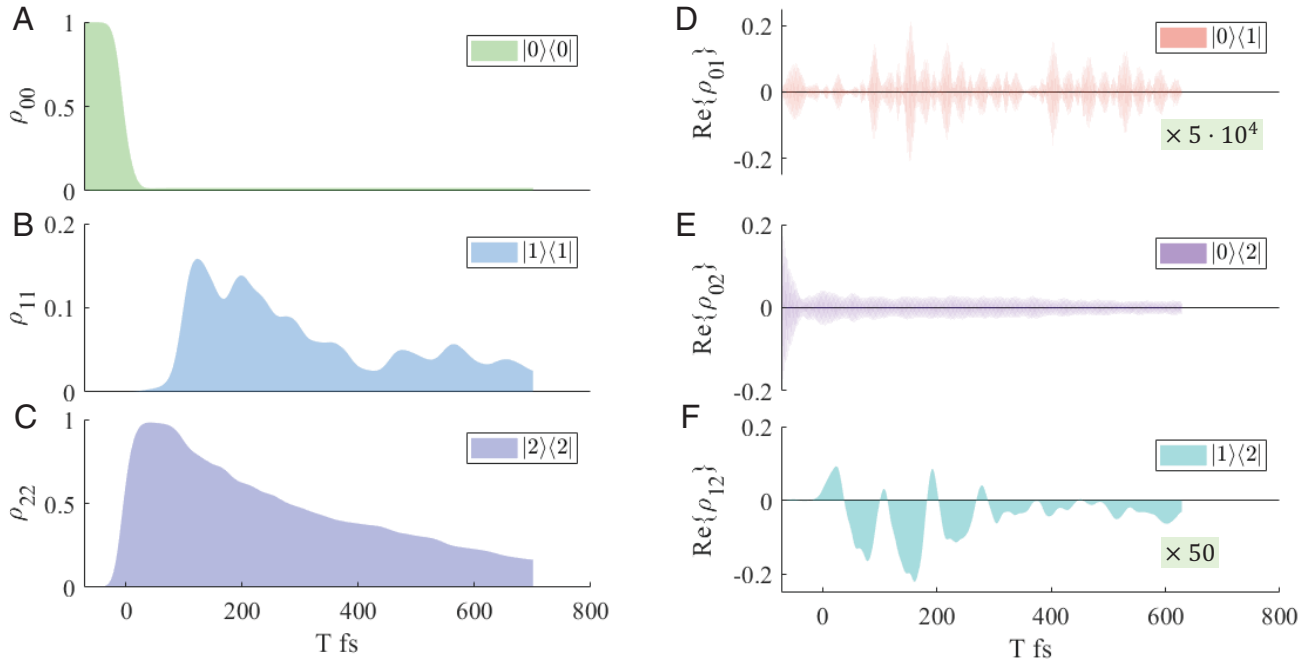

Fig. 3. Population and coherence dynamics. The molecule is initially in its ground state, depicted by the $|0\rangle\langle 0|$ population in *A*. Around $t = 100$ fs, the second excited state $|2\rangle$ is populated (*B*) followed by probability flow to state $|1\rangle$ (*C*). *D–F* present the real parts of the respective electronic coherence rescaled by the green highlighted prefactor for visibility.

first-order contribution (the imaginary part of the integration is taken). The coherences, on the other hand, are maximal at $k = k_0$ and thus, contribute. This results in a background-free electronic coherence signal on the zero-loss peak.

The overall signal obtained by the summation in Eq. **6** is depicted in Fig. 5. By comparing Fig. 4*F* with Fig. 5, it is evident that the $|1\rangle\langle 2|$ coherence dominates the signal. This coherence is developed during the dynamics around ≈ 180 fs when the molecule reaches the CoIn between these electronic states. It is evident from the numerical integration that the $|0\rangle\langle 2|$ and $|0\rangle\langle 1|$ coherences are not negligible, yet they contribute significantly less than the $|1\rangle\langle 2|$ coherence. The main reason for this is that the temporal resolution required to sample this oscillator is <0.4 fs and thus, seems to be averaged/filtered out.

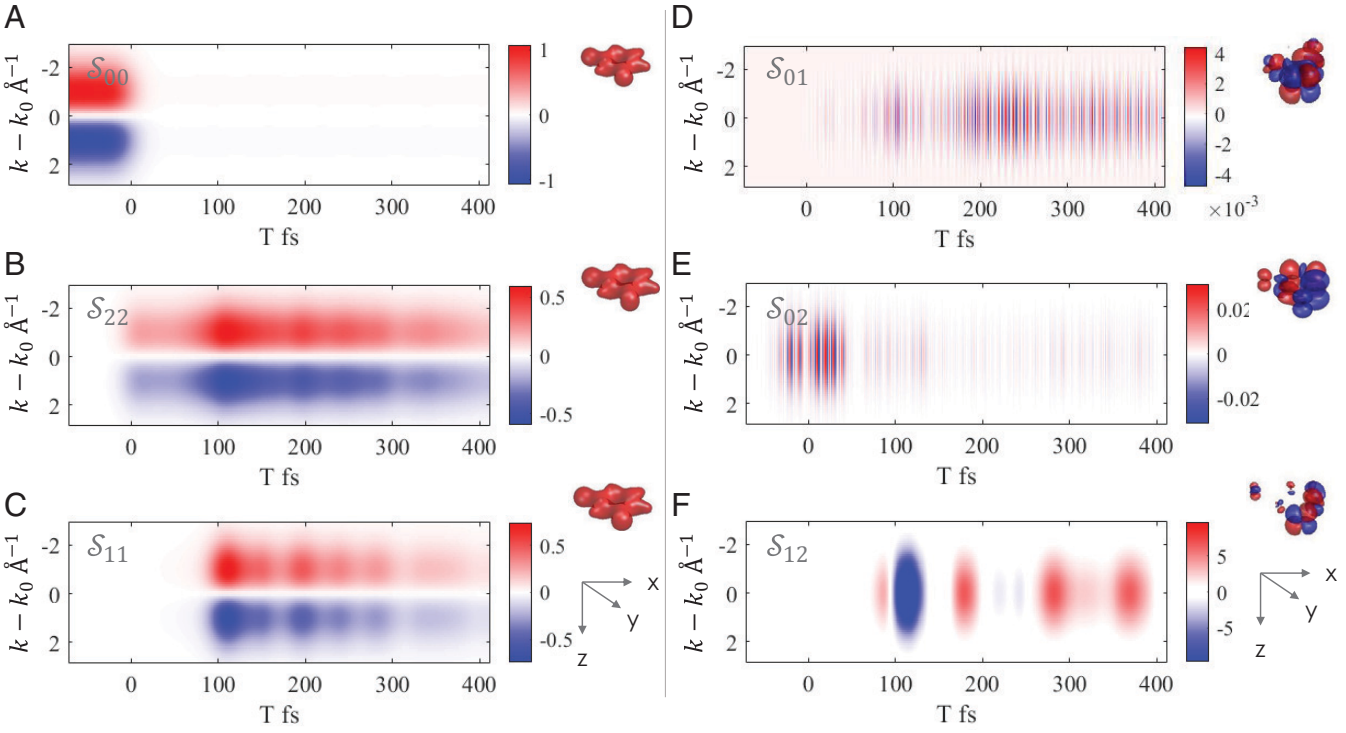

Fig. 4. Signal contributions. *A–C* depict the contributions to the signal in Eq. **6** from the diagonal contributions $\mathcal{S}_{ii}$ ($\sigma_{00}, \sigma_{11}, \sigma_{22}$, respectively), corresponding to the electron aligned along the *x* direction of the charge density, shown in *Right*. *D–F* depict the signals arising from the transition charge densities $\sigma_{01}, \sigma_{02}, \sigma_{12}$, respectively, corresponding to $\mathcal{S}_{ij}$, $(i \neq j)$ under similar conditions.

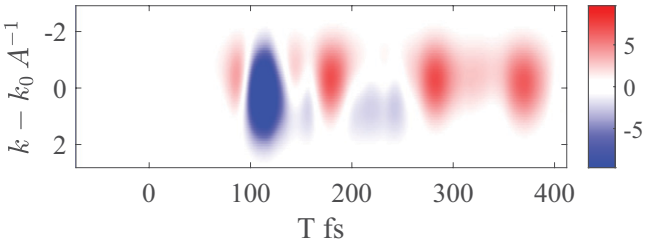

Fig. 5. Total signal. The recorded signal is obtained from superposition of all the contributing processes given by Eq. **6**.

The signal contributions in Fig. 4 exhibit temporal oscillations with different frequencies. These are especially pronounced for the coherences in Fig. 4 *D*–*F*, where the $|0\rangle\langle 2|$ and $|0\rangle\langle 1|$ contributions oscillate with higher frequency due to the energy difference between the adiabatic states, while the frequency of the $|1\rangle\langle 2|$ contribution that stems from the CoIn is lower. To characterize them further, we performed a temporal gating analysis inspired by a cross-correlation frequency-resolved optical gating (XFROG) measurement (25–35) according to

$$I_{\mathrm{FROG}}(\omega, T) = \left| \int_{-\infty}^{\infty} dt\, \mathcal{S}_{\boldsymbol{k}}(t) E_{\mathrm{gate}}(t - T)\, e^{-i\omega t} \right|^2, \quad [7]$$

where E_{gate} is a Gaussian function with a 3-fs FWHM and $\mathcal{S}(t)$ is a temporal signal trace taken at $k = k_0$ where the coherence dominates. I_{FROG} is numerically evaluated only at the postprocessing stage, requiring no additional measurements. It gives information about the transient frequency of the oscillations and is depicted in Fig. 6 for all contributions and the total signal.

While the population signatures are around zero frequency, the $|0\rangle\langle 1|$ and $|0\rangle\langle 2|$ coherences appear between 2 and 3 eV in Fig. 6 *D* and *E*. The energy difference between the adiabatic states is around 5 eV, where the discrepancy can be explained by evaluating the signal "only" every 1 fs and thereby, undersampling with respect to these fast oscillations. Nevertheless, they are well separated from the $|1\rangle\langle 2|$ coherence in Fig. 6*F*. This is the most interesting dynamical signature. It starts at 0.1 eV around 80 fs and then, splits into a constant signature staying at 0.1 eV and another one that decays to 0.01 eV at 120 fs. As discussed in ref. 23, the 20-fs pump pulse excites a local nuclear wave packet in S_2, which then travels to the CoIn. This arrival is directly mapped by the FROG spectogram in Fig. 6*F*. The $|1\rangle\langle 2|$ coherence emerges at 0.1 eV, where the nonadiabatic coupling between S_2 and S_1 already is nonvanishing. Part of it then travels to the actual crossing region where the energy difference between the adiabatic states is vanishing. The signal thus provides direct access to nuclear wave packet pathways in ultrafast molecular dynamics. The FROG of the total signal in Fig. 6*G* is dominated

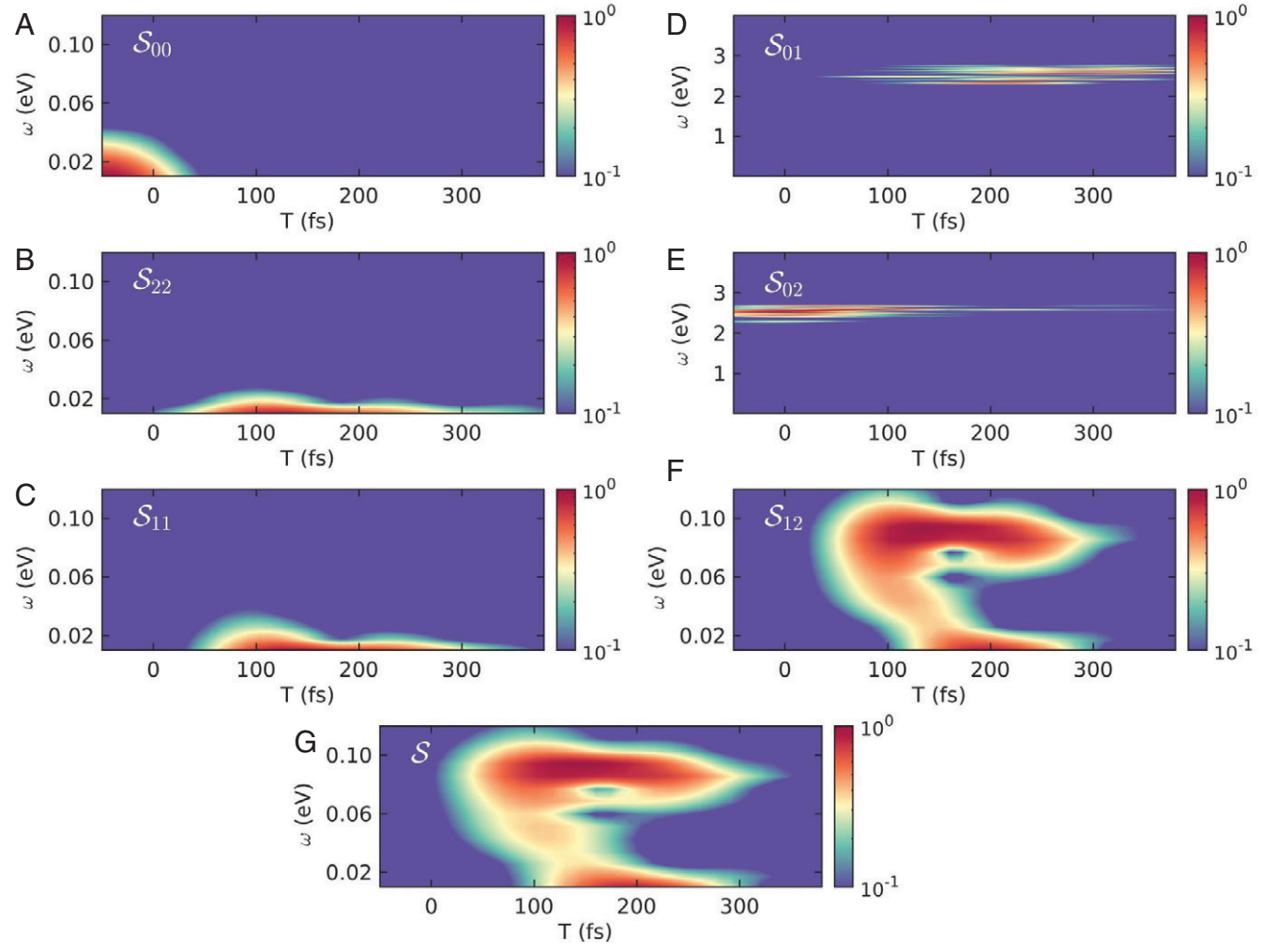

Fig. 6. XFROG analysis. Using Eq. **7** with $\mathcal{S}(t)$ taken at $k = k_0$ from the individual contributions, we depict the XFROG decomposition of the total signal. *A*–*C* correspond to XFROG spectrograms of the populations and *D*–*F* to the ones of the coherence contributions to the signal in Fig. 4. *G* presents the XFROG of the total signal in Fig. 5.

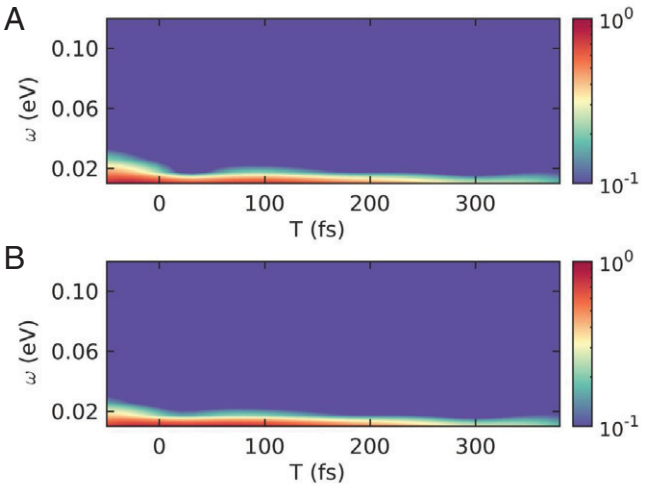

Fig. 7. XFROG analysis according to Eq. **7** with $\mathcal{S}(t)$ taken at $k = 2.8$ Å (*A*) and 5.6 Å (*B*) from the total signal in Fig. 5.

by this $|1\rangle\langle 2|$ contribution since we take the signal trace at $k = k_0$ where the populations are weak, allowing for direct access to the coherences. By gradually shifting $\mathcal{S}_k(t)$ to k values away from k_0, populations get more visible in the total XFROG and eventually, dominate. This is demonstrated in *SI Appendix* and constitutes a convenient and readily accessible analysis tool for both populations and coherences (Fig. 6).

Conclusions

SPICES is a technique that monitors electronic coherences of optically pumped aligned molecules in a background-free manner using frequency-resolved broadband electron and manifest heterodyne electron detection. The signal is maximal when the optical pulse propagates parallel to the electron beam. The temporal resolution of the nonadiabatic evolution is initiated by the optical pulse by scanning the delay time (T) between the optical pulse and the center of the free electron pulse. In the unfocused, collimated, broad-beam regime considered here (weak electron–sample coupling), the long-range longitudinal component (Coulomb term) is dominant, and due to the dispersive broadband nature of the coupling, the free electron's phase is significantly shaped by the coherence of the charge density.

The hybrid combination of electron and photon probes is particularly useful to monitor ultrafast coherence phenomena. The photonic degrees of freedom offer the well-developed quantum optical toolbox with unparalleled temporal control and weak nondestructive coupling as well as advanced generation and detection schemes (26–31). The electronic degrees of freedom present a highly versatile broadband source with unparalleled spatial resolution. The dispersive coupling—responsible for the electron's decoherence properties even in the weak coupling regime—is useful for sensing electronic coherences.

The weak coupling regime enabled the spatial extension of the electron pulse in the transverse plane (low effective cross-section). Therefore, the interaction can be interpreted as the interference of free electron trajectories recoiled by the long-ranged Coulomb term. This picture is related to the recently proposed "aloof spectroscopy" (32), whereby an electron beam is focused outside the sample, generating optical excitations that depend on the distance between the focusing point and the sample. Here, since the temporal resolution is important to sample the ultrashort electronic coherence, the entire free electron bandwidth is used.

The present signal corresponds to heterodyne detection of the generated electron field with the incoming beam. Ordinary EELS signals require two interactions with the incoming beam. Here, we only need one interaction, and the signal is given by its interference with the incoming beam. For photons, this is known as heterodyne detection. This signal is analogous to TRUECARS introduced in ref. 24, where the electron field is replaced by a photon field. In SPICES, the electronic coherence is more pronounced due to the long-ranged Coulomb potential.

For nonradiative decay pathways, such as CoIn, higher-order processes are not required. Generally, the relaxation process from the initial optical pump may be radiative, which will result in a resonant term $\propto (\boldsymbol{j}\cdot\boldsymbol{A})^2$ in the interaction Hamiltonian for the photon generation (Wigner–Weisskopf like). Interference between these two processes may also lead to interesting effects, although not studied in this work. Recently, some of these advantages were experimentally demonstrated, showing significant background reduction (pathway filtering) in energy-dispersive X-ray spectrometry (33). Moreover, photon–electron and electron–electron entanglement is expected to enhance pathway separation, introducing noise reduction mechanisms and joint time–frequency resolution that exceed the classical boundaries (34).

Data Availability. All study data are included in the article and/or *SI Appendix*.

ACKNOWLEDGMENTS. The support of NSF Grant CHE-1953045 is acknowledged. D.K. acknowledges the support of the Alexander von Humboldt Foundation through the Feodor Lynen Program. V.Y.C. and S.M. were supported by US Department of Energy, Office of Science, Basic Energy Sciences Award DE-SC0022134.

1. F. Carbone, O.-H. Kwon, A. H. Zewail, Dynamics of chemical bonding mapped by energy-resolved 4D electron microscopy. *Science* **325**, 181–184 (2009).
2. R. F. Egerton, Electron energy-loss spectroscopy in the TEM. *Rep. Prog. Phys.* **72**, 016502 (2008).
3. S. T. Park, M. Lin, A. H. Zewail, Photon-induced near-field electron microscopy (PINEM): Theoretical and experimental. *New J. Phys.* **12**, 123028 (2010).
4. D. J. Flannigan, B. Barwick, A. H. Zewail, Biological imaging with 4D ultrafast electron microscopy. *Proc. Natl. Acad. Sci. U.S.A.* **107**, 9933–9937 (2010).
5. F. J. García de Abajo, A. Asenjo-Garcia, M. Kociak, Multiphoton absorption and emission by interaction of swift electrons with evanescent light fields. *Nano Lett.* **10**, 1859–1863 (2010).
6. R. J. Glauber, M. Lewenstein, Quantum optics of dielectric media. *Phys. Rev. A* **43**, 467–491 (1991).
7. H. T. Dung, L. Knöll, D.-G. Welsch, Three-dimensional quantization of the electromagnetic field in dispersive and absorbing inhomogeneous dielectrics. *Phys. Rev. A* **57**, 3931–3942 (1998).
8. S. Y. Buhmann, *Dispersion Forces I* (Springer-Verlag, Berlin, Germany, 2012).
9. V. Chernyak, S. N. Volkov, S. Mukamel, Electronic structure-factor, density matrices, and electron energy loss spectroscopy of conjugated oligomers. *J. Phys. Chem. A* **105**, 1988–2004 (2001).
10. P. Baum, On the physics of ultrashort single-electron pulses for time-resolved microscopy and diffraction. *Chem. Phys.* **423**, 55–61 (2013).
11. M. Aidelsburger, F. O. Kirchner, F. Krausz, P. Baum, Single-electron pulses for ultrafast diffraction. *Proc. Natl. Acad. Sci. U.S.A.* **107**, 19714–19719 (2010).
12. W. Domcke, D. R. Yarkony, H. Köppel. *Conical Intersections* (World Scientific, 2011).
13. A. R. Attar *et al.*, Femtosecond x-ray spectroscopy of an electrocyclic ring-opening reaction. *Science* **356**, 54–59 (2017).
14. E. Tapavicza, A. M. Meyer, F. Furche, Unravelling the details of vitamin D photosynthesis by non-adiabatic molecular dynamics simulations. *Phys. Chem. Chem. Phys.* **13**, 20986–20998 (2011).
15. D. Polli, D. Brida, S. Mukamel, G. Lanzani, G. Cerullo, Effective temporal resolution in pump-probe spectroscopy with strongly chirped pulses. *Phys. Rev. A* **82**, 053809 (2010).
16. W. J. Schreier, P. Gilch, W. Zinth, Early events of DNA photodamage. *Annu. Rev. Phys. Chem.* **66**, 497–519 (2015).
17. A. Barlev, D. Sen, Catalytic DNAs that harness violet light to repair thymine dimers in a DNA substrate. *J. Am. Chem. Soc.* **135**, 2596–2603 (2013).
18. D. Geppert, L. Seyfarth, R. de Vivie-Riedle, Laser control schemes for molecular switches. *Appl. Phys. B* **79**, 987–992 (2004).
19. H. A. Wegner, Molecular switches. *Angew. Chem. Int. Ed.* **51**, 2281–2281 (2012).
20. M. Born, R. Oppenheimer, Zur quantentheorie der molekeln. *Ann. Phys.* **389**, 457–484 (1927).
21. D. Keefer, S. Thallmair, S. Matsika, R. de Vivie-Riedle, Controlling photorelaxation in uracil with shaped laser pulses: A theoretical assessment. *J. Am. Chem. Soc.* **139**, 5061–5066 (2017).
22. S. Matsika, M. Spanner, M. Kotur, T. C. Weinacht, Ultrafast relaxation dynamics of uracil probed via strong field dissociative ionization. *J. Phys. Chem. A* **117**, 12796–12801 (2013).
23. D. Keefer, T. Schnappinger, R. de Vivie-Riedle, S. Mukamel, Visualizing conical intersection passages via vibronic coherence maps generated by stimulated ultrafast X-ray Raman signals. *Proc. Natl. Acad. Sci. U.S.A.* **117**, 24069–24075 (2020).
24. M. Kowalewski, K. Bennett, K. E. Dorfman, S. Mukamel, Catching conical intersections in the act: Monitoring transient electronic coherences by attosecond stimulated x-ray Raman signals. *Phys. Rev. Lett.* **115**, 193003 (2015).

25. R. Trebino *et al.*, Measuring ultrashort laser pulses in the time-frequency domain using frequency-resolved optical gating. *Rev. Sci. Instrum.* **68**, 3277–3295 (1997).
26. S. Asban, K. E. Dorfman, S. Mukamel, Quantum phase-sensitive diffraction and imaging using entangled photons. *Proc. Natl. Acad. Sci. U.S.A.* **116**, 11673–11678 (2019).
27. S. Asban, D. Cho, S. Mukamel, Frequency-, time-, and wavevector-resolved ultrafast incoherent diffraction of noisy x-ray pulses. *J. Phys. Chem. Lett.* **10**, 5805–5814 (2019).
28. S. Asban, S. Mukamel, Scattering-based geometric shaping of photon-photon interactions. *Phys. Rev. Lett.* **123**, 260502 (2019).
29. S. Mukamel *et al.*, Roadmap on quantum light spectroscopy. *J. Phys. At. Mol. Opt. Phys.* **53**, 072002 (2020).
30. S. Asban, K. E. Dorfman, S. Mukamel, Interferometric spectroscopy with quantum light: Revealing out-of-time-ordering correlators. *J. Chem. Phys.* **154**, 210901 (2021).
31. S. Asban, S. Mukamel, Distinguishability and "which pathway" information in multidimensional interferometric spectroscopy with a single entangled photon-pair. *Sci. Adv.* **7**, eabj4566 (2021).
32. P. Rez *et al.*, Damage-free vibrational spectroscopy of biological materials in the electron microscope. *Nat. Commun.* **7**, 1–8 (2016).
33. D. Jannis, K. Müller-Caspary, A. Béché, A. Oelsner, J. Verbeeck, Spectroscopic coincidence experiments in transmission electron microscopy. *Appl. Phys. Lett.* **114**, 143101 (2019).
34. S. Asban, F. Javier García de Abajo, Generation, characterization, and manipulation of quantum correlations in electron beams. *NPJ Quantum Inf.* **7**, 42 (2021).
35. S. Linden, H. Giessen, J. Kuhl, XFROG? A new method for amplitude and phase characterization of weak ultrashort pulses. *Phys. Status Solidi* **206**, 119–124 (1998).

Supplementary Information for: "Sensing ultrashort electronic coherent beating at conical intersections by single-electron pulses"

Electron Energy Loss Spectroscopy: Quantum Electrodynamics Approach

Shahaf Asban,[1,*] Daniel Keefer,[1] Vladimir Y. Chernyak,[2,3,†] and Shaul Mukamel[1,‡]

[1] *Department of Chemistry and Physics & Astronomy, University of California, Irvine, California 92697-2025, USA*
[2] *Department of Chemistry, Wayne State University, 5101 Cass Ave, Detroit, Michigan 48202, USA*
[3] *Department of Mathematics, Wayne State University, 656 W. Kirby, Detroit, Michigan 48202, USA*

We build an approach to Electron Energy Loss Spectroscopy, based on Quantum Electrodynamics.

CONTENTS

* sasban@uci.edu
† chernyak@chem.wayne.edu
‡ smukamel@uci.edu

I. DERIVATION OF THE SPICES SIGNAL

In this section we derive an explicit expression for the SPICES signal, starting with a Quantum Electro-Dynamics (QED) approach, and further applying a set of approximations and simplifications. In non-relativistic QED one starts with a system of free charged particles (electrons and nuclei), which are coupled to quantum electromagnetic field, described by the vector $\boldsymbol{A}$ and scalar potentials. The classical action of such a system has standard form. While switching to the Hamilton formalism, one observes that the system has constraints of first kind (according to Dirac's classification) that have a form $E_0(\boldsymbol{r}) = 0$ and $\operatorname{div} \boldsymbol{E}(\boldsymbol{r}) - 4\pi\rho(\boldsymbol{r}) = 0$, where $E_0(\boldsymbol{r})$ is the momentum, conjugate to $A_0(\boldsymbol{r})$. Upon quantization the constraints of first kind can be applied to the system wavefunction, thus identifying the subspace of physical states, whose wavefunction do not depend on the scalar potential and have a prescribed dependence on the longitudinal component of the vector counterpart. As a result the system maps onto a set of charged particles interacting with each other via the Coulomb coupling, as well as interacting with the photons, represented by the transverse component of the vector potential. The above procedure is known as gauge invariant quantization.

In our case we have electrons in a sample under study, as well as in subsystem, e.g., a piece of normal metal, referred to as the reservoir, that serves as a source for the probe electrons. We should also introduce a source, responsible for the optical fields that drives the sample out of its equilibrium state, as well as an optical source creating a driving optical field, responsible for the photoionization processes, thus creating high-energy probe electrons. A source is represented by its time-dependent charge/current density $(\rho(\boldsymbol{r}, t), \boldsymbol{j}(\boldsymbol{r}, t))$ that satisfy the continuity equation $\partial_t \rho + \operatorname{div} \boldsymbol{r} = 0$, the latter ensuring gauge invariance of the interaction of the source with the scalar and vector potentials.

We will further introduce the following simplifications/approximations. Since the sample, reservoir, and probe electrons are well separated either in real, or energy-momentum space, we will describe them using three independent quantum fields. The Hamiltonian of the whole system can be, therefore, represented in a form

$$H(t) = H_0(t) + H^{int}(t), \quad H_0(t) = H_\mu(t) + H_f + H_s, \quad H^{int}(t) = H_\mu^{int} + H_s^{int}(t). \tag{1}$$

In Eq. (1) $H_0(t)$ includes the kinetic and Coulomb energy of the charged particles (electrons and nuclei) in the sample, the energy of the free transverse electromagnetic field (photons), coupling of the photons to the charged particles of the sample, as well as to the optical source, responsible to the sample driving field, as prescribed by QED; its time dependence originates from the optical source-photon coupling. The terms H_f and H_s represent the Hamiltonians of free probe electrons and electrons in the reservoir, respectively; H_μ represents Coulomb interactions between the probe and sample electrons, as well as coupling between the probe electrons and photons. Finally, $H_s^{int}(t)$ describes photoionization processes of converting the reservoir electrons to fast probe counterparts; this is a simplified description of photoionization, compared to the original QED version that uses an optical source of the photoionization field, coupled to the source and free electrons via transverse photons, obtained by invoking a classical approximation for the photoionizing field. The initial density matrix is naturally assumed in a factorized form

$$\varrho = \varrho_\mu \otimes \varrho_f \otimes \varrho_\mathrm{s}, \tag{2}$$

with ϱ_μ representing the canonical distribution of the material/sample (including photons) at some actual temperature T, ϱ_f represents a pure state with no electrons, while ϱ_s is an equilibrium state of the electron reservoir. A more detailed derivation of Eq. (1), based on the effective action formalism, will be published elsewhere.

Neglecting probe electron scattering on the sample excitations via a transverse photon exchange, i.e., limiting it to pure Coulomb, we have

$$H_\mu^{int} = \int d\boldsymbol{r} d\boldsymbol{r}' \frac{\sigma_\mu(\boldsymbol{r}')\sigma_f(\boldsymbol{r})}{|\boldsymbol{r} - \boldsymbol{r}'|}, \quad \sigma_f(\boldsymbol{r}) = -e\Psi^\dagger(\boldsymbol{r})\Psi(\boldsymbol{r}), \tag{3}$$

where $\sigma_\mu(\boldsymbol{r})$ is the charge density operator, associated with the sample, whereas $\Psi(\boldsymbol{r})$ and $\Psi^\dagger(\boldsymbol{r})$ are the probe electron annihilation and creation operators, respectively. The reservoir-probe electron coupling Hamiltonian can be represented in a form

$$H_s^{int}(t) = \int d\boldsymbol{r}(\Psi^\dagger(\boldsymbol{r})\Theta(\boldsymbol{r}, t) + \Theta^\dagger(\boldsymbol{r}, t)\Psi(\boldsymbol{r})), \tag{4}$$

where $\Theta(\boldsymbol{r}, t)$ and $\Theta^\dagger(\boldsymbol{r}, t)$ are time-dependent operators that represent collective reservoir variables, their time-dependence originates from the time dependence of the ionizing field.

In what follows we use the following standard convention: for a Hilbert space operator Q, we denote Q_α, with $\alpha = \mathrm{L}, \mathrm{R}, \pm$, the corresponding Liouville space operators, $Q_\alpha(t)$ is the Heisenberg (time-dependent) counterpart of Q_α with respect to Liouville space dynamics, associated with the Liouville operator $\mathcal{L} = H_-$, whereas $\tilde{Q}_\alpha(t)$ is the Heisenberg operator, associated with the Liouville operator $\mathcal{L}_0 = (H_0)_-$. It is convenient to consider the most general

signal, associated with counting the total number of beam electrons in a detector; it has a very simple form in terms of the Liouville-space correlation functions of the beam electron variables

$$\mathcal{S}(\boldsymbol{r},t;\boldsymbol{r}',t')) = \langle \Psi_{\rm L}(\boldsymbol{r},t)\Psi^{\dagger}_{\rm R}(\boldsymbol{r}',t')\rangle = {\rm Tr}({\rm T}(\Psi_{\rm L}(\boldsymbol{r},t)\Psi^{\dagger}_{\rm R}(\boldsymbol{r}',t'))(\varrho)), \quad \mathcal{S}(\boldsymbol{r},\boldsymbol{r}';t)) = \mathcal{S}(\boldsymbol{r},t;\boldsymbol{r}',t)) \tag{5}$$

where T denotes Liouville space chronological time ordering, and the time dependence of the operators in Eq. (5) is determined by the Heisenberg picture/formalism, as per the convention, described above. The time-integrated, momentum-resolved signal, considered in this paper, can be expressed in terms of the correlation function, introduced in Eq. (5), as

$$S_{\boldsymbol{k}} = \int_{-\infty}^{\infty} \bar{S}_{\boldsymbol{k}}(t) \quad \bar{S}_{\boldsymbol{k}}(t) = \int \frac{d\boldsymbol{k}'}{(2\pi)^3}\frac{d\boldsymbol{k}''}{(2\pi)^3} m_{\boldsymbol{k},\boldsymbol{k}'} m^{*}_{\boldsymbol{k},\boldsymbol{k}''} \int d\boldsymbol{r}' d\boldsymbol{r}'' e^{-i\boldsymbol{k}'\cdot\boldsymbol{r}'+i\boldsymbol{k}''\cdot\boldsymbol{r}''}\mathcal{S}(\boldsymbol{r}',\boldsymbol{r}'';t) \tag{6}$$

To perform perturbative computations, we recast Eq. (5) in the interaction picture, treating $H^{\rm int}$ in Eq. (1) as a perturbation to H_0

$$\mathcal{S}(\boldsymbol{r},t;\boldsymbol{r}',t')) = \left\langle \tilde{\Psi}_{\rm L}(\boldsymbol{r},t)\tilde{\Psi}^{\dagger}_{\rm R}(\boldsymbol{r}',t')\exp\left(-i\hbar^{-1}\int d\tau \tilde{H}^{int}_{-}(\tau)\right)\right\rangle. \tag{7}$$

Note that, by the definition of the Liouville space correlation functions, the operators under the angular brackets in Eq. (7) should be chronologically time-ordered, so that when expanding the exponential term in a Taylor series, one can disregard the non-commutative nature of operators. Since interaction between the sample/material system and the beam electrons is weak, due to the high energy of the free electrons, and the density of the beam electrons is low, we will look at the lowest orders of the perturbation theory providing a non-vanishing signal, which is first order in H^{int}_{μ} and second order in H^{int}_{s} [or, more specifically, it boils down to first order in $H^{int}_{s,{\rm L}}$ and first order in $H^{int}_{s,{\rm R}}$], thus providing the signal, linear in the density of beam electrons, so that Coulomb interaction between the latter can be neglected.

To obtain a closed formal expression for the signal, we note that within the approximation, described above, the expression in the r.h.s. of Eq. (7) contains one of each of the operators $\tilde{\sigma}_{\mu}$, $\Theta_{\rm L}$, and $\Theta_{\rm R}$ and 6 probe electron operators (3 creation plus 3 annihilation). Computing the 6-point Liouville space correlation function of the probe electrons by applying the Liouville space version of the Wick theorem, we arrive at the expression

$$\begin{aligned}&\mathcal{S}(\boldsymbol{r},\boldsymbol{r}';t)) = -\left(\frac{1}{\hbar}\right)^3 \int_{\mathbb{R}^3} d\tau d\tau_1 d\tau_2 \int_{X^{\times 3}} d\boldsymbol{r}_f d\boldsymbol{r}_1 d\boldsymbol{r}_2 u(\boldsymbol{r}_f,\tau)\\ &G(\boldsymbol{r},\boldsymbol{r}_f,t-\tau)G(\boldsymbol{r}_f,\boldsymbol{r}_1,\tau-\tau_1)(G(\boldsymbol{r}',\boldsymbol{r}_2,t-\tau_2))^{*}K(\boldsymbol{r}_1,\tau_1,\boldsymbol{r}_2,\tau_2) + {\rm c.c.},\end{aligned} \tag{8}$$

where

$$u(\boldsymbol{r}_f,t) = -e\int d\boldsymbol{r}_{\mu}\frac{\langle\tilde{\sigma}_{\mu}(\boldsymbol{r}_{\mu},t)\rangle}{|\boldsymbol{r}-\boldsymbol{r}_{\mu}|}, \tag{9}$$

is the Coulomb potential, associated with the photoinduced charge density in the sample, whereas G and K are the retarded correlation function of the probe beam electrons and the "population" correlation function of the reservoir collective variables, respectively:

$$G(\boldsymbol{r},\boldsymbol{r}';t-t') = -i\langle\tilde{\Psi}_{\rm L}(\boldsymbol{r},t)\tilde{\Psi}^{\dagger}_{\rm L}(\boldsymbol{r}',t')\rangle, \quad K(\boldsymbol{r},t;\boldsymbol{r}',t') = \langle\tilde{\Theta}_{\rm L}(\boldsymbol{r},t)\tilde{\Theta}^{\dagger}_{\rm R}(\boldsymbol{r}',t')\rangle. \tag{10}$$

Note that $G(\boldsymbol{r},\boldsymbol{r}';t) = 0$ for $t<0$, and $K(\boldsymbol{r},t;\boldsymbol{r}',t')$ completely describes the beam of high-energy probe electrons, and plays a role of some kind of dynamical spectral density of the high-energy electron source. In what follows, we will use the following explicit expression for the retarded correlation function of the probe electrons

$$G(\boldsymbol{r},\boldsymbol{r}';t) = -i\chi_{\mathbb{R}_+}(t)\int_{\mathbb{R}^3}\frac{d\boldsymbol{k}}{(2\pi)^3}e^{i\boldsymbol{k}\cdot(\boldsymbol{r}-\boldsymbol{r}')}e^{-i\varepsilon_{\boldsymbol{k}}t}, \quad \varepsilon_{\boldsymbol{k}} = \frac{\hbar\boldsymbol{k}^2}{2m}. \tag{11}$$

The expression in Eq. (8) can be further simplified under a very natural assumption that the electron reservoir is located far away enough from the experimental sample, so that there is a moment in time t_0, so that by that moment the ionizing pulse is gone [i.e., $H^{int}_{s}(t) = 0$, for $t > t_0$], whereas the probe electron wavepacket is still far enough fro the sample, so that we can set $H^{int}_{\mu}(t) = 0$, for $t < t_0$. This allows the time integration in Eq. (8) to be restricted to $\tau_1,\tau_2 \in (-\infty,t_0)$ and $\tau \in (t_0,t)$. Since the retarded Green function $G(\boldsymbol{r},\boldsymbol{r}';t)$ represents the kernel of the one-electron evolution operator, it possesses the time concatenation property, allowing Eq. (8) to be recast in a simpler form

$$\begin{aligned}&\mathcal{S}(\boldsymbol{r},\boldsymbol{r}';t)) = \frac{1}{\hbar}\int_{t_0}^{t} d\tau \int_{X^{\times 3}} d\boldsymbol{r}_f d\boldsymbol{r}_1 d\boldsymbol{r}_2 u(\boldsymbol{r}_f,\tau)\\ &G(\boldsymbol{r},\boldsymbol{r}_f,t-\tau)G(\boldsymbol{r}_f,\boldsymbol{r}_1,\tau-t_0)(G(\boldsymbol{r}',\boldsymbol{r}_2,t-t_0))^{*}\rho_f(\boldsymbol{r}_1,\boldsymbol{r}_2;t_0) + {\rm c.c.},\\ &\rho_f(\boldsymbol{r}_1,\boldsymbol{r}_2;t_0) = \left(\frac{1}{\hbar}\right)^2\int_{-\infty}^{t_0} d\tau_1 \int_{-\infty}^{t_0} d\tau_2 G(\boldsymbol{r}_1,\boldsymbol{r}'_1;t_0-\tau_1)(G(\boldsymbol{r}_2,\boldsymbol{r}'_2;t_0-\tau_2))^{*}K(\boldsymbol{r}'_1,\tau_1,\boldsymbol{r}'_2,\tau_2).\end{aligned} \tag{12}$$

where $\rho_f(\boldsymbol{r}_1, \boldsymbol{r}_2; t_0)$ should be viewed as a reduced one-electron density of the probe electron beam at time t_0, which represents all relevant properties of the probe electron source, in application to the considered signal in the lowest non-vanishing order of the perturbation theory, described above. Note that the relevant properties of the probe electron source are generally described by a one-electron mixed, rather than a pure state.

Summarizing, Eqs. (6), (12), and (9) together with Eq. (11) constitute a complete set of integral expressions for the signal considered in this paper. They clearly demonstrate that the dynamical information that can be retrieved from the considered spectroscopic measurement is the time- and position-dependent charge density, induced in the experimental sample upon photoexcitation.

The expression for the signal $S_{\boldsymbol{k}}$ can be further simplified by introducing the Fourier transform of the induced charge density and the probe electron reduced density matrix, i.e., expressing them latter as

$$\langle \tilde{\sigma}_\mu(\boldsymbol{r}, t)\rangle = \int_{-\infty}^{\infty} \frac{d\omega}{2\pi} \int_{\mathbb{R}^3} \frac{d\boldsymbol{q}}{(2\pi)^3} e^{-i\omega t + i\boldsymbol{q}\cdot\boldsymbol{r}} \sigma_\mu(\boldsymbol{q}, \omega), \tag{13}$$

and

$$\rho_f(\boldsymbol{r}_1, \boldsymbol{r}_2; t_0) = \int_{\mathbb{R}^3} \frac{d\boldsymbol{k_1}}{(2\pi)^3} \int_{\mathbb{R}^3} \frac{d\boldsymbol{k_2}}{(2\pi)^3} e^{i\boldsymbol{k}_1\cdot\boldsymbol{r}_1 - i\boldsymbol{k}_2\cdot\boldsymbol{r}_2} \rho_{\boldsymbol{k}_1\boldsymbol{k}_2}(t_0), \tag{14}$$

and further substituting Eqs. (13) and (14), together with the integral representation for the one-electron Green functions [Eq. (11)] into Eq. (12)) and further into Eq. (6). Then all spatial integration can be easily explicitly performed, resulting in the delta-functions, that reflect momentum conservation for all scattering processes involved resulting in:

$$\begin{aligned}\mathcal{S}_{\boldsymbol{k}} = \frac{ie}{\hbar} \int_{-\infty}^{\infty} \frac{d\omega}{2\pi} \int_{\mathbb{R}^3} \frac{d\boldsymbol{q}}{(2\pi)^3} \frac{\sigma_\mu(\boldsymbol{q}, \omega)}{\boldsymbol{q}^2} \int_{\mathbb{R}^3} \frac{d\boldsymbol{k}_1}{(2\pi)^3} \int_{\mathbb{R}^3} \frac{d\boldsymbol{k}_2}{(2\pi)^3} \rho_{\boldsymbol{k}_1-\boldsymbol{q},\boldsymbol{k}_2}(t_0) m_{\boldsymbol{k}\boldsymbol{k}_1} m^*_{\boldsymbol{k}\boldsymbol{k}_2} \\ \times \int_{t_0}^{\infty} dt e^{-\gamma t} \int_{t_0}^{t} d\tau e^{-i\varepsilon_{\boldsymbol{k}_1-\boldsymbol{q}}(\tau-t_0) - i\varepsilon_{\boldsymbol{k}_1}(t-\tau) + i\varepsilon_{\boldsymbol{k}_2}(t-t_0) - i\omega\tau} + \text{c.c.},\end{aligned} \tag{15}$$

where γ^{-1} represents the time window of collecting the time-integrated signal. Performing the time integration in the r.h.s. of Eq. (**??**), we arrive at

$$\begin{aligned}\mathcal{S}_{\boldsymbol{k}} = \frac{ie}{\hbar} \int_{-\infty}^{\infty} \frac{d\omega}{2\pi} \int_{\mathbb{R}^3} \frac{d\boldsymbol{q}}{(2\pi)^3} \frac{\sigma_\mu(\boldsymbol{q}, \omega)}{\boldsymbol{q}^2} e^{-i\omega t_0} \int_{\mathbb{R}^3} \frac{d\boldsymbol{k}_1}{(2\pi)^3} \int_{\mathbb{R}^3} \frac{d\boldsymbol{k}_2}{(2\pi)^3} \rho_{\boldsymbol{k}_1-\boldsymbol{q},\boldsymbol{k}_2}(t_0) m_{\boldsymbol{k}\boldsymbol{k}_1} m^*_{\boldsymbol{k}\boldsymbol{k}_2} \\ \times \frac{1}{\varepsilon_{\boldsymbol{k}_2} - \varepsilon_{\boldsymbol{k}_1} + i\gamma} \frac{1}{\varepsilon_{\boldsymbol{k}_2} - \varepsilon_{\boldsymbol{k}_1-\boldsymbol{q}} - \omega + i\gamma}.\end{aligned} \tag{16}$$

To understand clearly the dependence of the signal on t_0, in deriving Eq. (15), we switched to the variables $t \mapsto t - t_0$ and $\tau \mapsto \tau - t_0$; we also assumed $\gamma|t_0| \ll 1$ and dropped such terms that occurred in the exponential.

We further assume that (i) $m_{\boldsymbol{k}\boldsymbol{k}_1}$, as a function of $\boldsymbol{k}_1$, is strongly peaked at $\boldsymbol{k}$ with a width Δk, and is normalized to unity, (ii) the probe electron wavepacket spectral width is large compared to Δk, which allows setting $\rho_{\boldsymbol{k}_1-\boldsymbol{q},\boldsymbol{k}_2} = \rho_{\boldsymbol{k}-\boldsymbol{q},\boldsymbol{k}}$, and (iii) $\boldsymbol{q}$ to be small enough to allow decomposing $\varepsilon_{\boldsymbol{k}_1-\boldsymbol{q}}$ to just first order in $\boldsymbol{q}$. We also follow the convention, adopted in this paper to describe the probe electron wavepacket at time T, described as the time when the optical pulse completely leaves the experimental sample, which boils down to setting $t_0 = T$, and $\rho_{\boldsymbol{k}_1\boldsymbol{k}_2}(t_0) = \rho_{\boldsymbol{k}_1\boldsymbol{k}_2}$, so that Eq. (16) adopts a form

$$\begin{aligned}\mathcal{S}_{\boldsymbol{k}}(T) = \frac{2e}{\hbar} \text{Im} \int_{-\infty}^{\infty} \frac{d\omega}{2\pi} e^{-i\omega T} \int_{\mathbb{R}^3} \frac{d\boldsymbol{q}}{(2\pi)^3} \frac{\sigma_\mu(\boldsymbol{q}, \omega)}{\boldsymbol{q}^2} \rho_{\boldsymbol{k}-\boldsymbol{q},\boldsymbol{k}} F(\boldsymbol{q}, \omega), \\ F(\boldsymbol{q}, \omega) = \int_{\mathbb{R}^3} \frac{d\boldsymbol{k}_1}{(2\pi)^3} \int_{\mathbb{R}^3} \frac{d\boldsymbol{k}_2}{(2\pi)^3} m_{\boldsymbol{k}\boldsymbol{k}_1} m^*_{\boldsymbol{k}\boldsymbol{k}_2} \frac{1}{\varepsilon_{\boldsymbol{k}_2} - \varepsilon_{\boldsymbol{k}_1} + i\gamma} \frac{1}{\varepsilon_{\boldsymbol{k}_2} - \varepsilon_{\boldsymbol{k}_1} + \boldsymbol{v}_{\boldsymbol{k}_1}\cdot\boldsymbol{q} - \omega + i\gamma}.\end{aligned} \tag{17}$$

In the case of a perfect momentum resolution in the detector, or more specifically $(\Delta k)v \ll \gamma$, we can set $\boldsymbol{k}_1 = \boldsymbol{k}_2$ in the resonant factors in the second line of Eq. (17) to obtain a simpler expression, we are using in this paper

$$\mathcal{S}_{\boldsymbol{k}}(T) = \frac{2e}{\hbar\gamma} \text{Re} \int_{-\infty}^{\infty} \frac{d\omega}{2\pi} e^{-i\omega T} \int_{\mathbb{R}^3} \frac{d\boldsymbol{q}}{(2\pi)^3} \frac{\sigma_\mu(\boldsymbol{q}, \omega)}{\boldsymbol{q}^2} \frac{1}{\boldsymbol{v}\cdot\boldsymbol{q} - \omega + i\gamma} \rho_{\boldsymbol{k}-\boldsymbol{q},\boldsymbol{k}} \tag{18}$$

In the main text we consider a case when the initial probe electron wave-packet is represented by a pure state.

II. NUMERICAL DETAILS

The Hamiltonian setup for uracil photorelaxation has been described in Refs. **(author?)** [2, 3]. Electronic structure calculations were performed on the CASSCF/MRCIS level of theory as implemented in the program package MOLPRO **(author?)** [8], using an active space of 12 electrons in 9 orbitals (5 π, one Oxygen lone pair, and 3 π^* orbitals). All quantities including the potential energy surfaces, (transition) dipole moments and non-adiabatic couplings were computed in 2-dimensional nuclear space spanned by the displacement vectors from the Franck-Condon point to the S_2/S_1 CoIn and to the local S_2 minimum, respectively. These coordinates had been identified by theory to capture the relevant wavepacket motion in the S_2 state and through the S_2/S_1 CoIn **(author?)** [3**?**].

For the nuclear wavepacket dynamics, these quantities are discretized on a numerical grid spanning 256 grid points in both dimensions. The time-dependent Schrödinger equation is solved numerically using a Chebychev propagation scheme **(author?)** [6] with a time step of 0.05 fs The effective Hamiltonian in matrix form comprising three electronic states is given by

$$\hat{H} = \begin{pmatrix} \hat{T} + \hat{V}_{S_0}(\mathbf{R}) & 0 & -\hat{\mu}_{02}E(t) \\ 0 & \hat{T} + \hat{V}_{S_1}(\mathbf{R}) & \hat{K}_{12} \\ -\hat{\mu}_{20}E(t) & \hat{K}_{21} & \hat{T} + \hat{V}_{S_2}(\mathbf{R}) \end{pmatrix}, \tag{19}$$

where $\hat{V}$ are the potential energy surfaces. The kinetic energy operator $\hat{T}$ in Eq. 19 is given in the G-Matrix formalism **(author?)** [1, 7] according to

$$\hat{T} \simeq -\frac{\hbar^2}{2m} \sum_{o=1}^{2} \sum_{p=1}^{2} \frac{\partial}{\partial q_o} \left[G_{op} \frac{\partial}{\partial q_p} \right] \tag{20}$$

with $o, p \in \mathbf{R}$ and the G-Matrix computed via its inverse elements

$$\left(G^{-1}\right)_{op} = \sum_{i=1}^{3N} m_i \frac{\partial x_i}{\partial q_o} \frac{\partial x_i}{\partial q_p} \quad . \tag{21}$$

The terms $\hat{K}_{ij}$ in Eq. 19 approximate the non–adiabatic couplings and are given by**(author?)** [4]

$$\hat{K}_{ij} = \frac{1}{2m} \left(2 f_{ij} \frac{\partial}{\partial \mathbf{R}} + \frac{\partial}{\partial \mathbf{R}} f_{ge} \right) \tag{22}$$

with f_{ij} containing terms $\langle \Phi_i | \ \frac{\partial}{\partial \mathbf{R}} \Phi_j \rangle$ with the electronic wavefunction Φ. Since the only CoIn contained in our Hamiltonian is between S_2 and S_1, the other non-adiabatic couplings are set to zero. The dipolar coupling element $\hat{\mu}E(t)$ enables laser excitation from S_0 to the optically bright S_1 with the laser field $E(t)$, whereas the $S_0 \rightarrow S_1$ transition is optically dark.

The nuclear wavefunction $\chi(\mathbf{R}, t)$ is obtained by propagating the S_0 ground state vibrational wavefunction $\chi(\mathbf{R}, t_0)$. Excitation to S_2 is performed by a 20 fs FWHM laser field tuned to the S_0A Butterworth filter **(author?)** [5] was employed in S_1 that absorbs the wavepacket reaching the S_1minimum. This is done to create an artificial exit channel and avoid artifacts, since our Hamiltonian is not suited to describe the wavepacket path in S_1 and the CoIns leading to S_0 are not contained. The filter was of "right-pass" type (absorbing all parts on the left side of the border), and placed at $q_1 = 0.5$ Å with an order of 100.

III. ELECTRON AND NUCLEAR DENSITIES

To calculate the signal in Equation 1 of the main text, electronic and nuclear densities of the molecule are required. They were calculated on a 18x15 grid in the nuclear space. Electron densities were evaluated from the state-specific charge density matrices P_{rs}^{ij} according to

$$\sigma_{ij}^{E}(\mathbf{q}, \mathbf{R}) = \int dr e^{-i\mathbf{q}\cdot\mathbf{r}} \sum_{rs} P_{rs}^{ij}(\mathbf{R}) \phi_r^*(\mathbf{r}, \mathbf{R}) \phi_r(\mathbf{r}, \mathbf{R}) \quad , \tag{23}$$

using the basis set of atomic orbitals $\phi_r(\mathbf{r})$. All electrons of uracil contribute to the diagonal state densities σ_{ii}, while the transition density consists of one electron located participating in the electronic transition (i.e. $n_O\pi^*$ for

$S_0 \rightarrow S_1$and $\pi\pi^*$ for $S_0 \rightarrow S_2$at the Franck-Condon point, while this changes across the nuclear space and especially around the CoIn).

The nuclear charge density for a given nuclear structure $\mathbf{R}$ in $\mathbf{q}$-space was calculated as

$$\sigma^N(\boldsymbol{q}, \boldsymbol{R}) = \sum_a Z_a e^{i\boldsymbol{q}\cdot\boldsymbol{R}_a}(\boldsymbol{R}) \tag{24}$$

where a labels the ath atom with atomic number Z_a at position $\mathbf{R}_a(\mathbf{R})$.

[1] P. H. Berens and K. R. Wilson. Molecular dynamics and spectra. I. Diatomic rotation and vibration. *The Journal of Chemical Physics*, 74(9):4872–4882, may 1981.

[2] D. Keefer, T. Schnappinger, R. de Vivie-Riedle, and S. Mukamel. Visualizing conical intersection passages via vibronic coherence maps generated by stimulated ultrafast X-ray Raman signals. *Proceedings of the National Academy of Sciences*, 117(39):24069–24075, sep 2020.

[3] D. Keefer, S. Thallmair, S. Matsika, and R. de Vivie-Riedle. Controlling Photorelaxation in Uracil with Shaped Laser Pulses: A Theoretical Assessment. *Journal of the American Chemical Society*, 139(14):5061–5066, apr 2017.

[4] S. Reiter, D. Keefer, and R. de Vivie-Riedle. Exact Quantum Dynamics (Wave Packets) in Reduced Dimensionality. In *Quantum Chemistry and Dynamics of Excited States*, pages 355–381. Wiley, nov 2020.

[5] Stephen Butterworth. On the Theory of Filter Amplifiers. *Experimental Wireless and the Wireless Engineer*, 7(6):536–541, 1930.

[6] H. Tal-Ezer and R. Kosloff. An accurate and efficient scheme for propagating the time dependent Schrödinger equation. *The Journal of Chemical Physics*, 81(9):3967–3971, nov 1984.

[7] S. Thallmair, M. K. Roos, and R. de Vivie-Riedle. Design of specially adapted reactive coordinates to economically compute potential and kinetic energy operators including geometry relaxation. *The Journal of Chemical Physics*, 144(23):234104, jun 2016.

[8] H.-J. Werner, P. J. Knowles, G. Knizia, F. R. Manby, M. Schütz, and Others. MOLPRO, version 2019.2, a package of ab initio programs, 2019.